BAMS Article

Storms and Precipitation Across the continental Divide Experiment (SPADE)

Julie M. Thériault, Nicolas R. Leroux, Ronald E. Stewart, André Bertoncini, Stephen J. Déry, John W. Pomeroy, Hadleigh D. Thompson, Hilary Smith, Zen Mariani, Aurélie Desroches-Lapointe, Selina Mitchell, and Juris Almonte

ABSTRACT: The Canadian Rockies are a triple-continental divide, whose high mountains are drained by major snow-fed and rain-fed rivers flowing to the Pacific, Atlantic, and Arctic Oceans. The objective of the April–June 2019 Storms and Precipitation Across the continental Divide Experiment (SPADE) was to determine the atmospheric processes producing precipitation on the eastern and western sides of the Canadian Rockies during springtime, a period when upslope events of variable phase dominate precipitation on the eastern slopes. To do so, three observing sites across the divide were instrumented with advanced meteorological sensors. During the 13 observed events, the western side recorded only 25% of the eastern side's precipitation accumulation, rainfall occurred rather than snowfall, and skies were mainly clear. Moisture sources and amounts varied markedly between events. An atmospheric river landfall in California led to moisture flowing persistently northward and producing the longest duration of precipitation on both sides of the divide. Moisture from the continental interior always produced precipitation on the eastern side but only in specific conditions on the western side. Mainly slow-falling ice crystals, sometimes rimed, formed at higher elevations on the eastern side (>3 km MSL), were lifted, and subsequently drifted westward over the divide during nonconvective storms to produce rain at the surface on the western side. Overall, precipitation generally crossed the divide in the Canadian Rockies during specific spring-storm atmospheric conditions although amounts at the surface varied with elevation, condensate type, and local and large-scale flow fields.

KEYWORDS: Field experiment; Mixed precipitation; Moisture/moisture budget; Orographic effects; Storm environments; Mountain meteorology

https://doi.org/10.1175/BAMS-D-21-0146.1

Corresponding author: Julie M. Thériault, theriault.julie@uqam.ca

In final form 26 August 2022

AFFILIATIONS: Thériault, Leroux, Thompson, and Desroches-Lapointe—Centre ESCER, Department of Earth and Atmospheric Sciences, Université du Québec à Montréal, Montreal, Quebec, Canada; **Stewart**—Department of Environment and Geography, University of Manitoba, Winnipeg, Manitoba, Canada; **Bertoncini and Pomeroy**—Centre for Hydrology, University of Saskatchewan, Canmore, Alberta, Canada; **Déry and Almonte**—Department of Geography, Earth and Environmental Sciences, University of Northern British Columbia, Prince George, British Columbia, Canada; **Smith**—Department of Earth and Atmospheric Sciences, Université du Québec à Montréal, Montreal, Quebec, and Department of Geography, Earth and Environmental Sciences, University of Northern British Columbia, Prince George, British Columbia, Canada; **Mariani**—Meteorological Research Division, Environment and Climate Change Canada, Toronto, Ontario, Canada; **Mitchell**—Natural Resources and Environmental Studies Program, University of Northern British Columbia, Prince George, British Columbia, Canada

The Canadian Rockies form a triple-continental divide, separating drainage basins to the Arctic, Pacific, and Atlantic Oceans (Fig. 1). Their high, partly glacierized peaks are the water towers for rivers that support vast areas of western Canada and northwestern United States; in total, 17% of North America lies within river basins receiving water from this region.

The region's hydrology is dominated by a long, cold, snowy winter from October through March, followed by the melt of the seasonal snow cover from April to July; this latter period is also associated with peak precipitation, which may fall as rain or snow. This wet period is then followed by a drier late summer period during which streamflow is dominated by groundwater discharge, glacier melt, and rainfall runoff.

This pattern of hydrology is sensitive to atmospheric features and change. From a continental scale, a small spatial shift of storm tracks along the continental divide can lead to substantial changes in the fraction of precipitation draining to the Pacific Ocean, Arctic Ocean, and Atlantic Ocean (Rood et al. 2005). Extreme spring and early summer precipitation events coinciding with snowmelt-driven freshets are common in the southern Canadian Rockies. They often lead to major flooding events such as in June 2013 (Pomeroy et al. 2016), impacting the local economy, infrastructure, agriculture, and tourism.

A key governing factor to continental-scale hydrology is the amount of moisture aloft crossing the Canadian Rockies's portion of the continental divide. Additionally, landfalling atmospheric rivers directly impact western coastal areas, bringing abundant precipitation to the region (Sharma and Déry 2020). The eastern slopes of the mountains, although associated with a dry climate, can be subject to heavy precipitation from westward moisture fluxes traveling from the Canadian Prairies and the interior United States, sometimes resulting in massive spring flooding (Pomeroy et al. 2016; Flesch and Reuter 2012). The June 2013 flood in southwestern Alberta (AB) and southeastern British Columbia (BC), which was one of the most expensive natural disasters in Canadian history at the time (Liu et al. 2016; Kochtubajda et al. 2016; Whitfield and Pomeroy 2016), provides a good example. During this event, moisture crossed the continental divide from southern AB into southeastern BC.

Extreme flooding events in the region are often due to rain-on-snow augmenting streamflow while a transition from rainfall to snowfall can mitigate that effect (Pomeroy et al. 2016a,b; Whitfield and Pomeroy 2016; Vionnet et al. 2020). Precipitation phase estimation is thus critical for flood forecasting. For example, during the 2013 flood, the Global Environmental Multiscale (GEM) model (Girard et al. 2014; McTaggart-Cowan et al. 2019), which is the

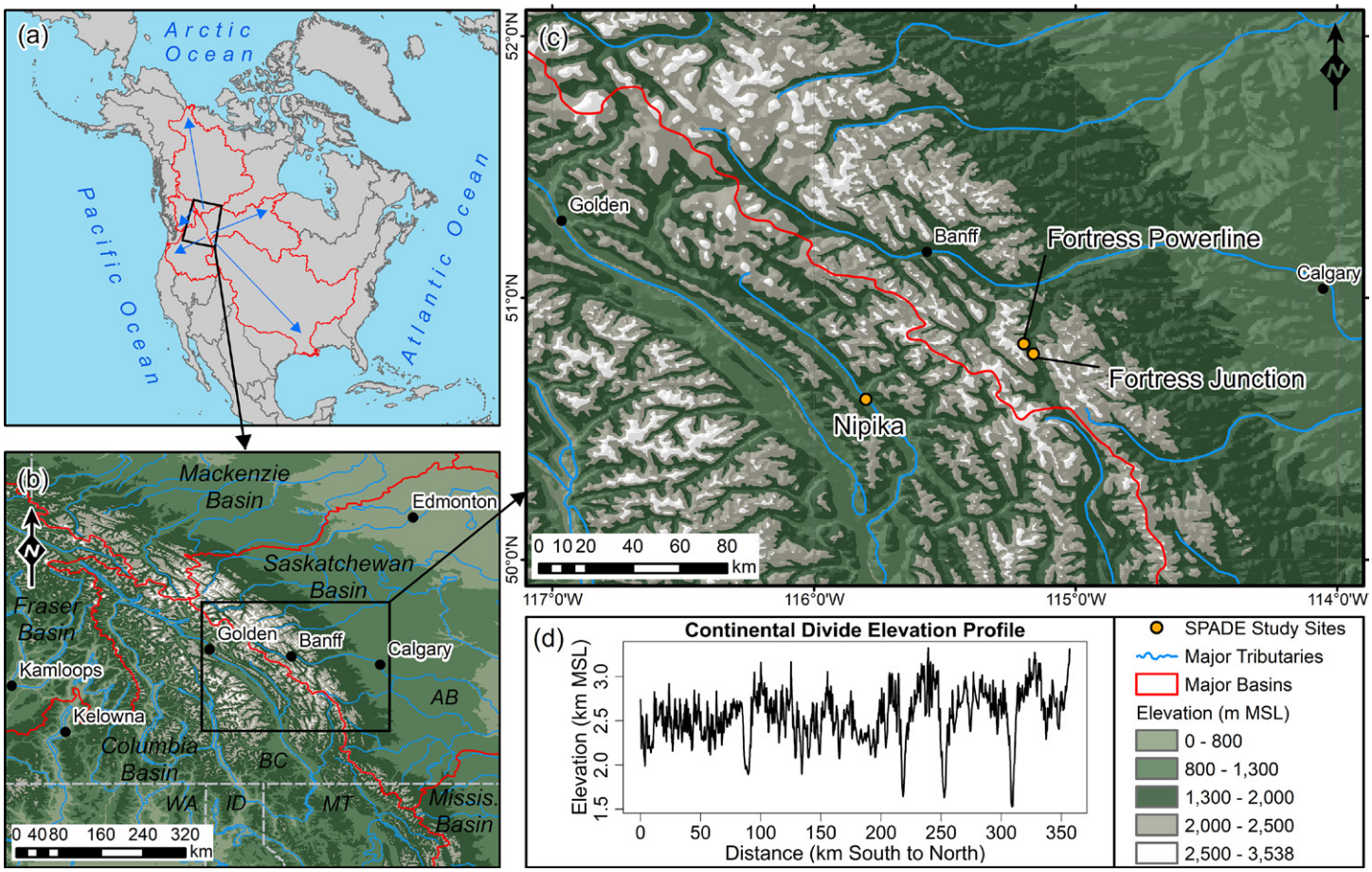

Fig. 1. Study region map showing (a) the major river basins (red outlines) of North America with respect to the Canadian Rockies, with the blue arrows indicating the direction in which surface water flows; (b) the Canadian Rockies and major headwater basins; (c) the study domain; and (d) the continental divide elevation profile represented by the red line in (c). All data used in this map are from the U.S. Geological Survey (USGS).

Canadian numerical weather prediction model, did not accurately capture the amount and phase of precipitation over the southern Canadian Rockies, resulting in an underestimation of the forecasted streamflow.

Numerous factors influence where and what type of precipitation reaches the surface in mountainous regions. In addition to the large-scale environment, these include atmospheric stability (Minder et al. 2011), wind, temperature, and moisture patterns in proximity to the topography, as well as features of the associated precipitation aloft such as hydrometeor densities and fall velocities (e.g., Morales et al. 2019; Poirier et al. 2019). Near-surface humidity patterns are also important; solid precipitation, often rimed, can reach the surface at temperatures up to 8°C within dry ambient conditions (Harder and Pomeroy 2013; Thériault et al. 2018).

Rain–snow transitions and snow formation have been studied in mountainous regions across different parts of the world. In North America, such processes were explored in the Sierra Nevada (Marwitz 1986), in Washington State during the Improvement of Microphysical Parameterization through Observations Verification Experiment (IMPROVE; Stoelinga et al. 2003) and the Olympic Mountains Experiment (OLYMPEX; Houze et al. 2017), in the Canadian Coast Mountains during the Science of Nowcasting Winter Weather for the Vancouver 2010 Olympics (SNOW-V10; Isaac et al. 2014), and in the Rocky Mountains of Idaho State (Tessendorf et al. 2018). Studies in other continents include, for example, the Swiss Alps (Steiner et al. 2003) and the Haituo Mountains north of Beijing (Ma et al. 2017). To the best of our knowledge, none of those projects focused on the processes associated with precipitation crossing a continental divide.

Despite the importance of precipitation of varying phases across the continental divide in the southern Canadian Rockies, little is known about the atmospheric processes in this extreme event-prone region, and few observations linking surface meteorological features, precipitation, and atmospheric conditions have been obtained. This problem is not unique to this region; Lundquist et al. (2019) pointed out that there is a general need to improve the observation of precipitation in complex terrain. Consequently, the goal of the Storms and Precipitation Across the continental Divide Experiment (SPADE) is to investigate atmospheric conditions and processes leading to precipitation at and across the continental divide in the southern Canadian Rockies. The scientific issues are as follows:

- What are the atmospheric conditions leading to moisture and condensate crossing or being impeded by the continental divide?
- What storm types lead to precipitation falling on one or both sides of the divide?
- What are the precipitation characteristics at the surface within these different storm types?

SPADE was conducted from 24 April to 26 June 2019 across the border between AB and BC. This period climatologically covers precipitation being a mixture of rain and snow and annual maximum amounts, which sometimes lead to extreme events (Liu et al. 2016). The objective of this article is to describe the design and implementation of SPADE and to present and synthesize its findings.

Field project design and implementation

Study sites. The study region lies along the continental divide that forms the southern border between BC and AB, Canada, encompassing sections of Banff, Kootenay, and Yoho National Parks and Kananaskis Country (Fig. 1). Mount Assiniboine is the highest peak within the area, with an elevation of 3,618 m above mean sea level (MSL).

To quantify storms and precipitation across the continental divide, observational sites were installed on both sides within the study area (Fig. 2). Two sites were located at Fortress Mountain Snow Laboratory, AB, about 30 km east of the divide, at both high and midelevations

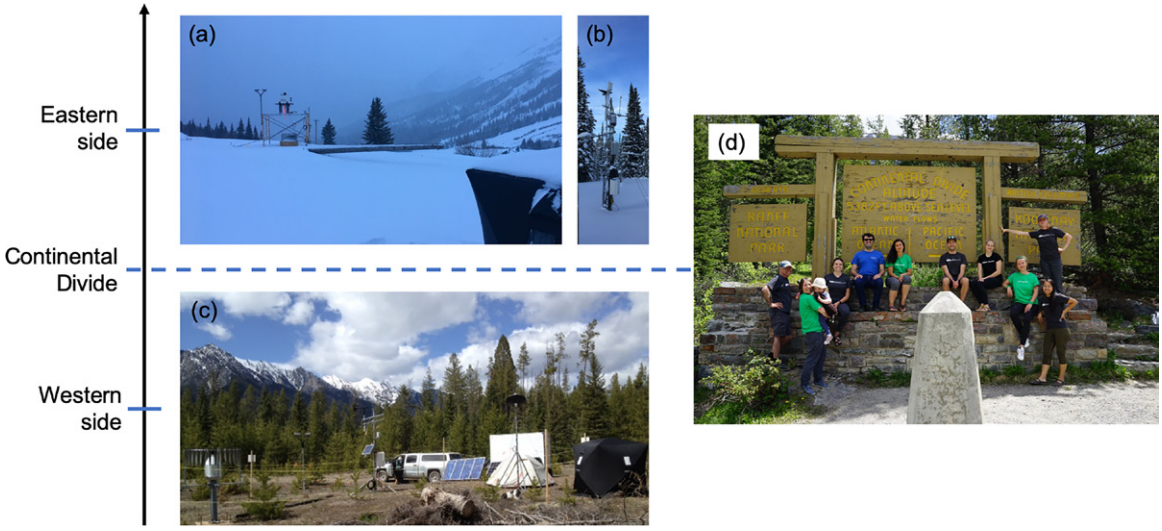

Fig. 2. The Storms and Precipitation Across the continental Divide Experiment (SPADE) experimental design. Two meteorological stations were deployed east of the continental divide at Fortress Powerline and Fortress Junction. (a) The meteorological station and (b) the Micro Rain Radar and the precipitation gauge (not shown in the photo) at Fortress Powerline. Similar instruments were also deployed at Fortress Junction. One meteorological site was deployed west of the divide at Nipika. (c) The Nipika site. All three sites are described in detail in Thériault et al. (2021). (d) A photo of SPADE participants at the continental divide during a sunny day.

(Fortress Powerline at 2,076 m MSL and Fortress Junction at 1,580 m MSL, respectively). A third site was located on the western side at Nipika Mountain Resort (Nipika at 1,087 m MSL), BC, about 30 km west of the divide. A description of the data collected during the experiment is given in Thériault et al. (2021).

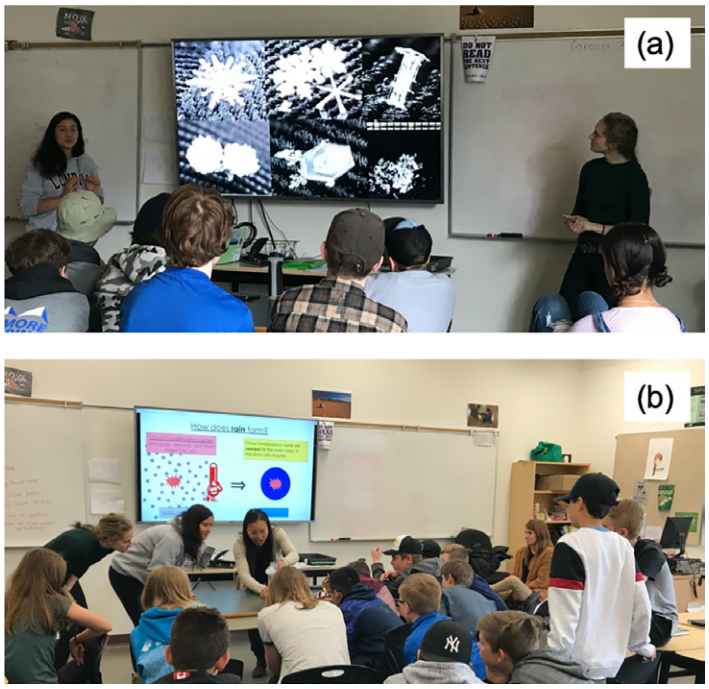

Fig. 3. SPADE students and project coordinator conducted outreach activities during SPADE with sixth graders at a middle school in Canmore, AB.

Observers on site. A group of nine undergraduate and graduate students were actively involved in the design, preparation, and conduct of the field experiment, with guidance from research faculty and a project coordinator. Their involvement was crucial to address technical challenges and to install instruments. For example, the site at Nipika was located in a remote area and the students had to design the solar panel system to power all instruments, including the Micro Rain Radar and the optical-laser disdrometer.

Manual observations were collected during storms on either side of the divide by the students. These included macrophotography of solid precipitation particles and reporting precipitation phase and types at Fortress Powerline and Nipika simultaneously (see sidebar). To determine the observational period, students also produced daily forecasts and shared them with all participants. Timing of the observations was then decided by consensus. Forecast discussion and storms documented were all posted on a blog (gwf-spade.weebly.com).

During sunny days, students shared their knowledge with the local community. Short courses on water, extreme events, and the experiment were given to sixth grade classes (Fig. 3). Community members were fascinated by the topic because they remembered the extreme flooding event of June 2013.

Instrumentation. The instrumentation and data collected during SPADE were introduced in Thériault et al. (2021). At all sites, air temperature, relative humidity, wind speed and direction, as well as precipitation amount and type at the surface were measured at a minimum frequency of 5 min. Characteristics of the precipitation were derived from automatic measurements of particle fall speed and size at all sites using an optical-laser disdrometer (Battaglia et al. 2010; Angulo-Martínez et al. 2018). Using theoretical fall speeds of raindrops, wet/rimed snow and dry snow, the relative fraction of each precipitation type was diagnosed (appendix A).

Vertically pointing Micro Rain Radars (MRR) were used to measure reflectivity and particle Doppler velocity, which is the vertical velocity relative to the ground of precipitation condensate aloft. The depth of the precipitation layer was characterized using reflectivity information. Particle growth process and phase changes were analyzed using both reflectivity and particle Doppler velocity. For example, the height of the melting level is identified at levels with a maximum reflectivity aloft associated with high vertical gradients of particle

Snowflake macrophotography

Documentation of solid hydrometeors at the surface is essential to better understand their formation mechanisms and to improve their representation in models. Nevertheless, no instrument can precisely measure crystal type characteristics or precipitation phase automatically, hence the development of photographic methods to document hydrometeor form is useful. Early records of snowflake photography come from Wilson A. Bentley, a farmer living in Jericho, Vermont. He photographed up to 5,000 snowflakes between 1885 and 1931, none of which were identical (Bentley and Humphreys 1962). Bentley used a feather to transfer the ice crystals to a microscope to be photographed without being damaged. Since the 1950s, many ice crystal habit-classification tables have been developed, including Nakaya (1954) and Kobayashi (1957). These tables have been used worldwide to identify the environmental conditions in which the various types of ice crystals grow. Manual observations and photography therefore enhance automated data by providing insight on the shapes and types of precipitation particles, which consequently allow one to infer associated atmospheric conditions aloft. With the evolution of technology, the photography setup from Bentley has been updated. It is now possible to easily build a macrophotography setup using a digital single-lens reflex camera and, for example, with a 60-mm macro lens (Fig. SB1). This can be used to document single ice crystals or a population of precipitation particles. A micro lens attached to a smartphone can also be used, as shown by Kumjian et al. (2020). Recently, the multi-angle snowflake camera (MASC) offers the possibility to analyze snowflakes by capturing high-resolution images of crystals as they fall (Garrett et al. 2012). Manual observations of precipitation particles provide an ideal opportunity for students and atmospheric scientists to learn firsthand about the complexity of particle shapes, densities, and sizes. To do so, precipitation particles are collected on a black velvet pad, for example, every 10 min when the environmental temperature is <0°C. The collection pad is then placed under the lens and a series of nine independent images are taken to capture all the particles on the pad. The photographic database can then be analyzed poststorm where ice crystal types and sizes are recorded in addition to parameters such as the degree or riming and/or occurrence of aggregations. Overall, manual photography still has many benefits. Human observers can identify unusual precipitation particles or the presence of particles smaller than what automated instruments can measure. It is now easier than ever to do and its analysis is much easier with digital imagery. Observers, experienced or not, are usually humbled by the complexity of the individual particles and by the wide diversity of particles that often fall simultaneously. This important type of measurement still has an important role in today's world.

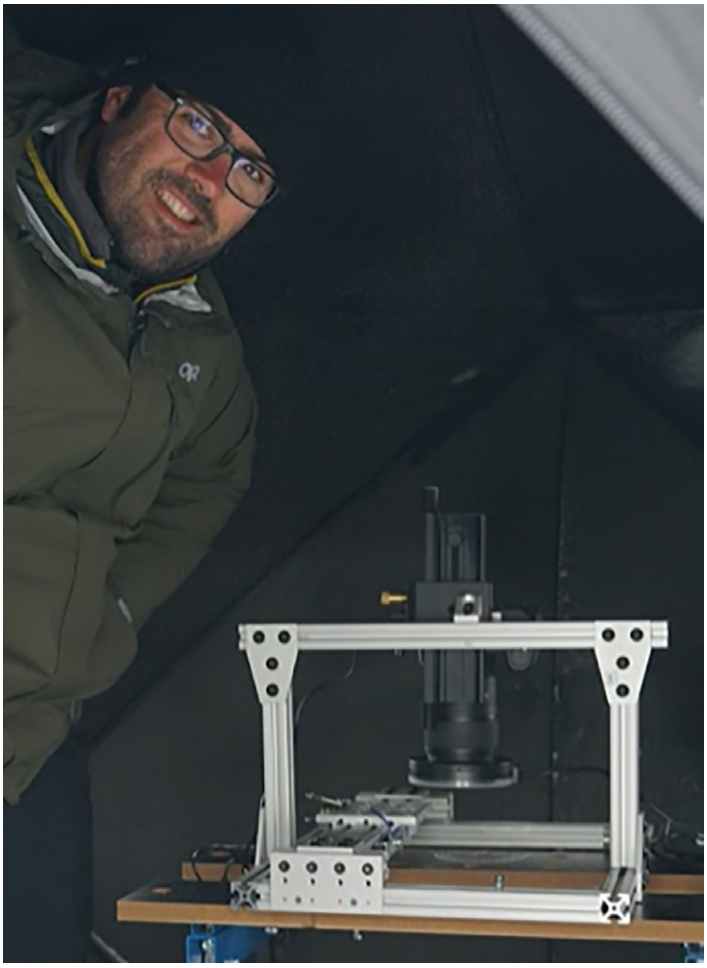

Fig. SB1. Field participant (André Bertoncini) with the macro photography setup installed in an ice fishing tent.

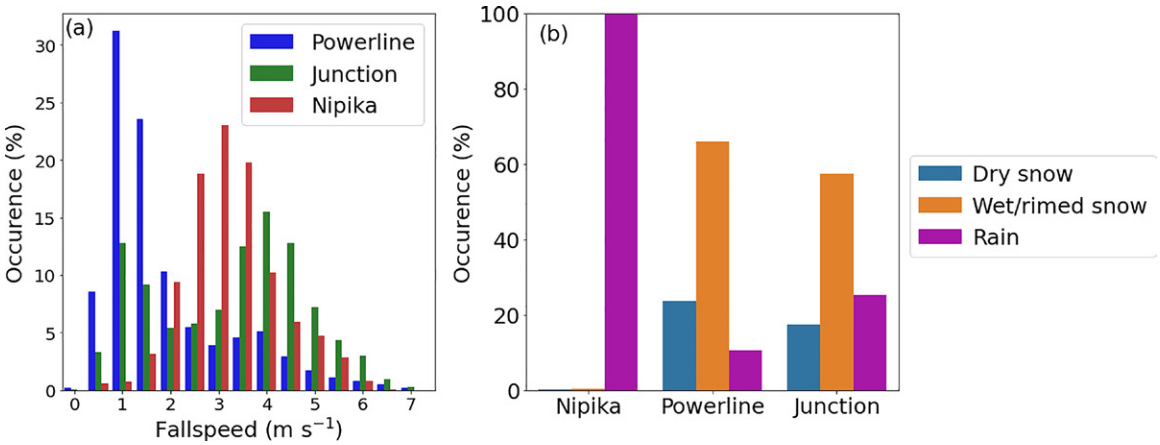

Fig. 4. (a) Occurrence (%) of fall speed values (bins of 0.5 m s^{-1}) at all three sites and (b) occurrence (%) of precipitation types diagnosed using the fall speeds and diameters measured with the optical-laser disdrometer.

Doppler velocity. This combination between reflectivity and Doppler velocity can indicate slow-falling particles, such as snow, melting into faster-falling particles, such as rain. The local flow field in association with precipitation initiation in the planetary boundary layer was measured with an all-sky scanning Doppler lidar.

Other datasets. To complete the SPADE dataset, the fifth generation of the ECMWF atmospheric reanalysis (ERA5; Hersbach et al. 2020) was used to create surface and upper-air analysis charts of mean sea level pressure, 1,000–500-hPa thickness, 10-m winds, and 500-hPa geopotential height. Moisture and condensate fluxes were also computed from this dataset (appendix B).

Storms and precipitation documented during SPADE

Overview of air temperature and precipitation at the surface. Atmospheric conditions varied across the continental divide during SPADE. Owing in part to its lower elevation, Nipika was on average 3.5° and 5.8°C warmer than Fortress Junction and Fortress Powerline, respectively. When reduced to the same elevation as Nipika, however, Fortress Powerline and Junction were generally warmer than Nipika, depending on the assumed lapse rate used (appendix C). Temperature differences also varied from storm to storm. This may be related to higher occurrences of clear skies at Nipika (9.7%) compared to Fortress Powerline (4.3%).

Between 24 April and 26 June 2019, 13 precipitation events were documented (appendix C). Total liquid equivalent accumulated precipitation was 195 and 133 mm at Fortress Powerline and Fortress Junction, respectively. In contrast, Nipika received only 71 mm. This period was slightly drier than the 1981–2010 climatology, in particular on the western side (Environment and Climate Change Canada 2021). Four precipitation events with accumulations > 20 mm at Fortress Powerline were classified as major events (events 1, 5, 9, and 13) while the other nine were minor events. Nine events on the western side had precipitation amounts < 5 mm.

Liquid precipitation was almost exclusively reported on the warmer western side compared to solid precipitation on the cooler eastern side (Fig. 4). The reported precipitation phase corresponded to the distribution of fall speeds measured by the optical-laser disdrometers; faster falling particles were mainly measured at Nipika compared to Fortress Powerline.

Photos of ice crystals taken during six precipitation events at Fortress Powerline, chosen to demonstrate the various habits and features, are shown in Fig. 5. Solid precipitation particles occurred either as single crystals, in various aggregated forms, or as a variety of combinations

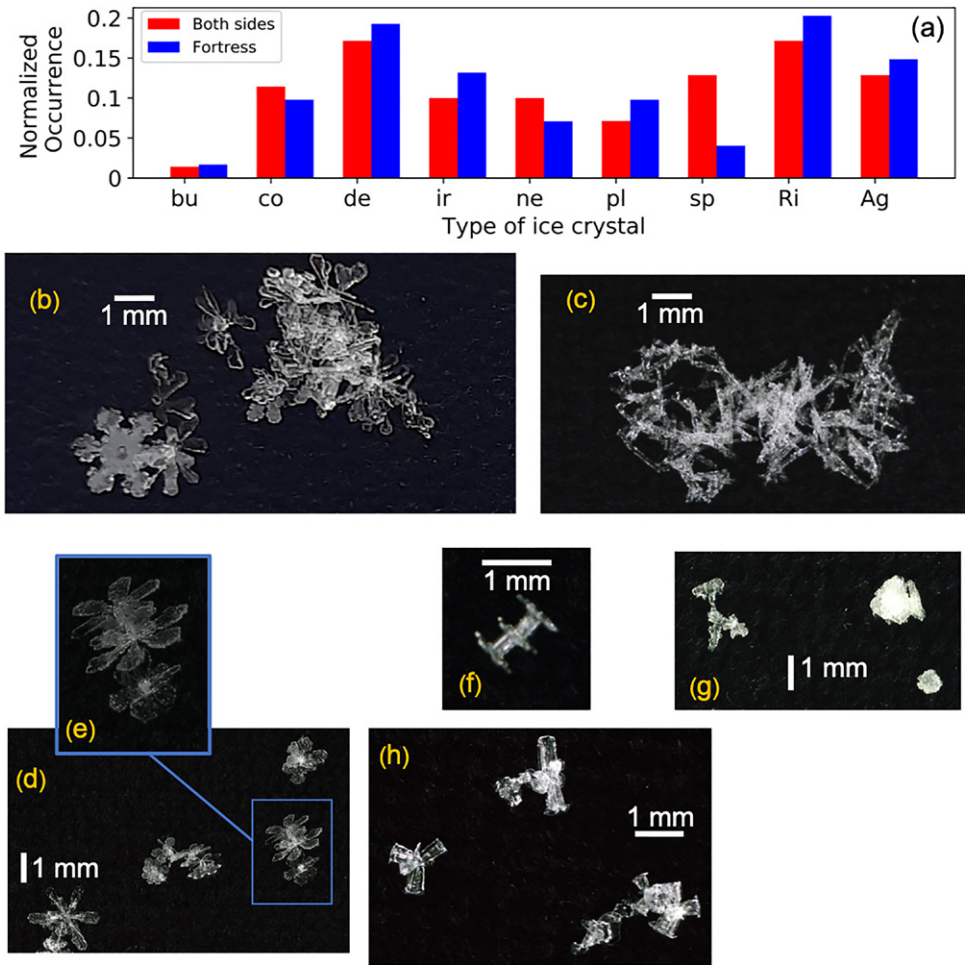

Fig. 5. (a) The 30-min normalized occurrence (number of counts with respect to each color category) of various types of ice crystals, riming degree (Ri) and aggregation (Ag) during the entire field project when precipitation only occurred on the eastern side (Fortress, blue bars) and when precipitation crossed the continental divide (both sides, red bars). Note that mainly rain reached the surface at Nipika. The types of ice crystals observed were bullets (bu), columns (co), dendrites (de), irregular (ir), needles (ne), plates (pl), and snow pellets (sp). They also occurred concurrently. (b)–(h) Example images of ice crystals and aggregates taken during event 5 using macrophotography equipment. Panels (b) and (c) are examples of aggregates of stellar plates (1040 UTC 16 May 2019) and needles (1443 UTC 17 May 2019), respectively, (d) shows a combination of stellar-type habit, including (e) showing a capped dendrite (0240 UTC 18 May 2019), (f) is a double capped column (1401 UTC 18 May 2019), (g) is a combination of graupel and refrozen wet snow (1941 UTC 18 May 2019), and (h) shows bullet rosettes that had different sizes (1541 UTC 18 May 2019). The scale is indicated in each panel.

of habit growth such as capped columns, capped dendrites, radial plates, and bullet rosettes. The most common type during all events was dendritic. They were followed by irregulars, columns, and plates. Bullets only occurred during events 1 and 13 (not shown). The occurrence of snow pellets was lower than most other types of precipitation although ice crystals were often rimed.

Overview of atmospheric conditions. The 13 precipitation events were categorized based on synoptic patterns and the direction of the incoming moisture flux toward the study area. The weather patterns identified in SPADE were similar to findings from Moran et al. (2007) and Sinclair and Marshall (2009). They studied meteorological conditions leading to precipitation over Haigh Glacier, AB, and Opabin Glacier, BC, located in the southern Canadian Rockies using stable-isotope signals.

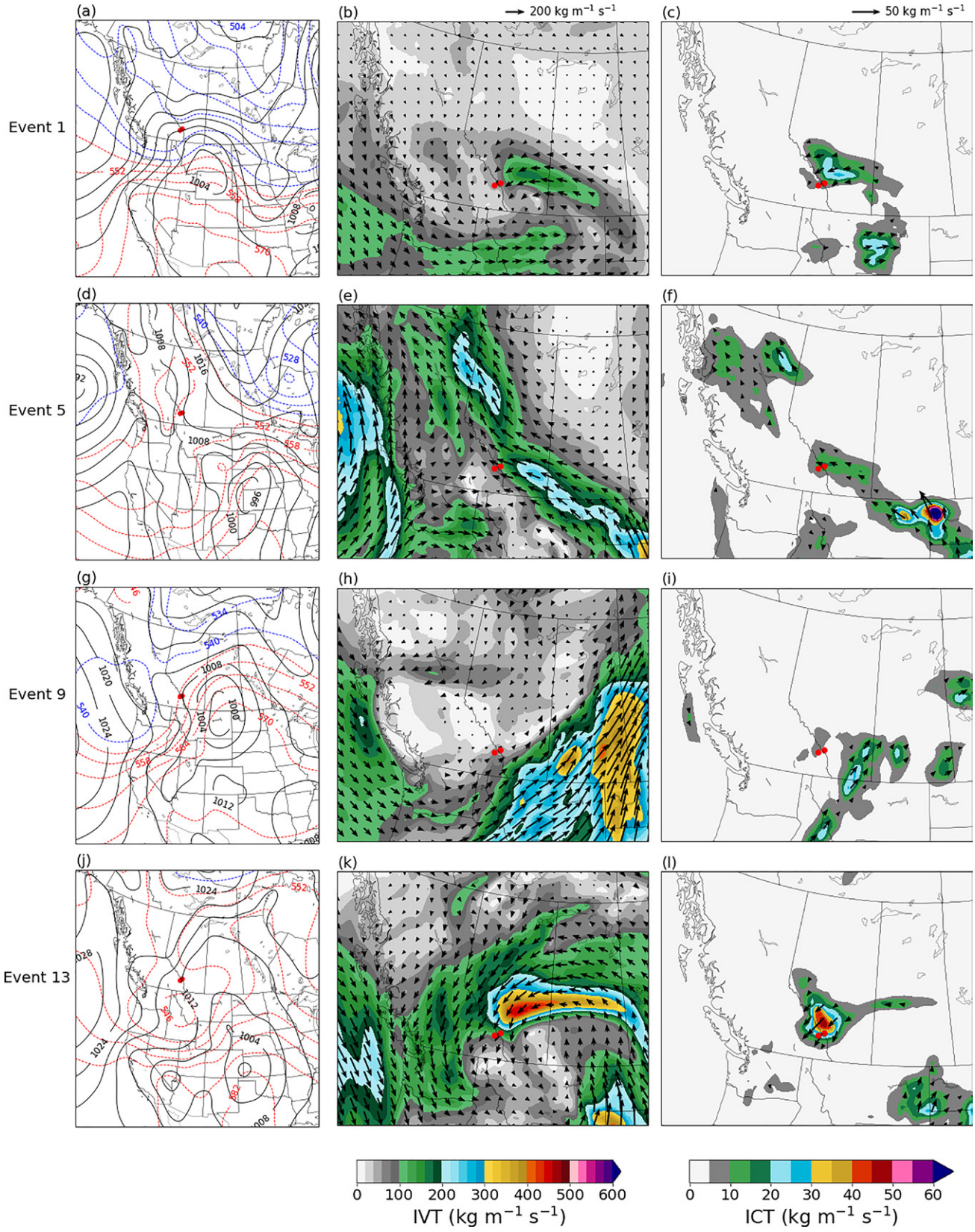

Fig. 6. Synoptic-scale atmospheric conditions during the four major events; these are (a)–(c) event 1 at 0000 UTC 28 Apr 2019, (d)–(f) event 5 at 0000 UTC 18 May 2019, (g)–(i) event 9 at 0600 UTC 7 Jun 2019, and (j)–(l) event 13 at 0600 UTC 21 Jun 2019. (left) The sea level pressure (black lines), the 1,000–500 hPa thicknesses that are ≤540 dam (blue dashed lines) and >540 dam (red dashed lines); (center) the distributions of vertically integrated moisture flux vector (Q; arrows) and its magnitude (IVT, color shaded); and (right) the distributions of vertically integrated condensate flux vector (Q_c; arrows) and its magnitude (ICT; color shaded) during the four major storms computed with ERA5. Times were chosen during the four major events near the onset of precipitation on the eastern side of the divide. Note that the domain used for (a), (d), (g), and (j) is different from the other panels. The variables used in this figure are detailed in appendix B.

Four major precipitation events were documented (Fig. 6). Six events (1, 6, 7, 9, 12, and 13) were associated with westward flow on the eastern slopes, moisture fluxes coming from the Canadian Prairies (eastern Alberta, Saskatchewan, and Manitoba), and low pressure systems located southeast of the SPADE domain. Four events (2, 4, 8, and 10) had moisture originating from the northwest, parallel to the divide, with low pressure systems located north of the SPADE domain. Two events (3 and 11) were associated with a low pressure system in northwestern Canada transporting moisture across BC. Finally, event 5 was unique and occurred after an atmospheric river landfall on the California coast; during that event, moisture from the Gulf of Mexico and the Pacific Ocean merged over the interior United States, and flowed northwestward, parallel to the Rocky Mountains (Fig. 6e).

Examples of meteorological conditions and precipitation aloft during westward moving precipitation events are shown in Fig. 7. On 27–28 April 2019 (event 1), a snowstorm produced 33 mm of liquid water equivalent at Fortress Powerline while only <2 mm (unknown type) reached the western side. In contrast, on 21 June 2019 (event 13), snow transitioned to rain at Fortress Powerline and Fortress Junction, and Nipika received 37% of the measured precipitation at Fortress Powerline during this event. The precipitation layer from MRR measurements was higher at Fortress Powerline during event 13 than during event 1.

The highest precipitation amounts produced at Nipika that did not come from the eastern side occurred during event 9, which was the only event that produced only ~5 mm difference between Fortress Powerline and Nipika. Event 9 was divided into two precipitation periods. For the first 14 h of that event, precipitation reached Nipika only, although detectable radar reflectivity values occurred aloft above Fortress Powerline. During the second period, reflectivity values increased significantly, and solid precipitation was measured at the surface at Fortress Powerline. During that time, the low pressure system produced southwestward low-level flow favorable for orographic lifting and precipitation on the eastern slopes of the Canadian Rockies.

Similarities in the wind patterns prior to precipitation were found (Fig. 8). From the Fortress Junction Doppler lidar velocity–azimuth display (VAD) scans (Lhermitte and Atlas 1961; Browning and Wexler 1968), the flow was mainly eastward and laminar above the continental divide (>3,500 m MSL). At lower vertical levels, the flow was northwestward with turbulent eddies. While the smooth laminar flow quickly transitioned to complex turbulent flow aloft prior to event 1, almost no change was observed during event 5. Winds blowing up-valley during event 5 were consistent with the constant moisture flux flowing northward along the mountain slopes. During event 9, winds above the continental divide were stronger and more laminar than within the valley, where they remained relatively calm. In contrast to event 1, winds were relatively calm and experienced almost no changes during both events 12 and 13.

Moisture and condensate fluxes across the continental divide

Moisture fluxes. Approximately 60% of the total accumulated precipitation on the eastern side was produced during the six events with a westward component of the moisture flux (Fig. 9). The moisture flux during events 6 and 7 came initially from northern AB and traveled southwestward. During events 1 and 12, the moisture flux originated off the Washington State coast, traveled eastward, and was recirculated westward over the Canadian Prairies by cyclonic flow across southeastern AB. The second half of event 9, and the entirety of event 13, were similar to events 1 and 12 but the moisture originated off the Californian coast. During the first half of event 9, the moisture traveled northeastward perpendicular to the divide and was farther north than during other storms, producing precipitation at Nipika before Fortress. Precipitation at both Fortress stations

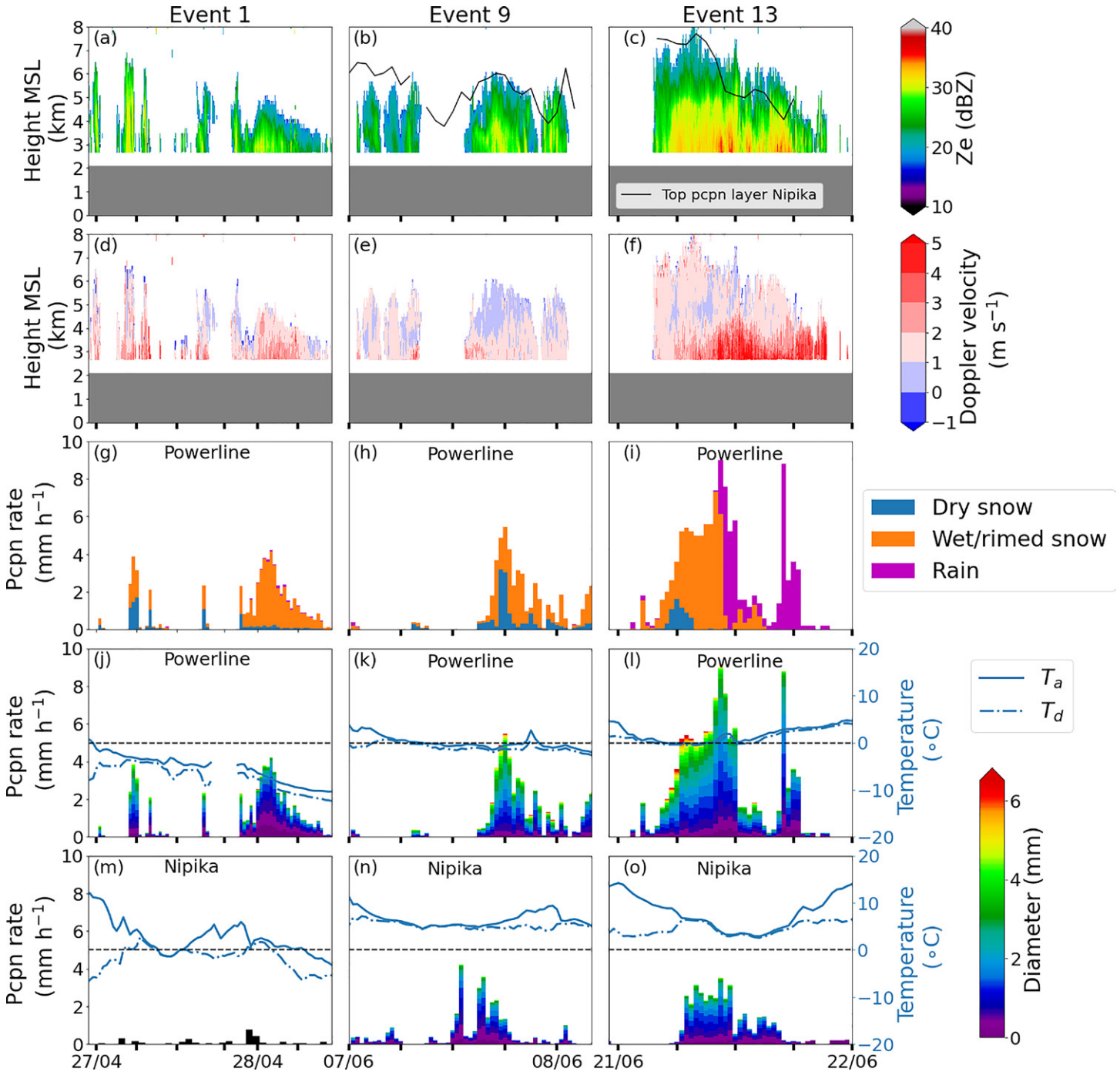

Fig. 7. Time series of (a)–(c) the Micro Rain Radar (MRR) reflectivity fields at 10-s intervals, including the 5-dB*Z* height of the Nipika MRR (black line), (d)–(f) MRR particle Doppler velocity fields at 10-s intervals, (g)–(i) precipitation amounts and types at Fortress at 30-min intervals, and (j)–(o) the precipitation rate, particle diameters, air temperature (T_a), and dewpoint temperature (T_d) on both sides of the continental divide. The dashed horizontal line in (j)–(o) is the 0°C isotherm. In particular, (j)–(l) are from Fortress Powerline on the eastern side and (m)–(o) are from Nipika on the western side. Note that the MRR and optical-laser disdrometer at Nipika were not operational during event 1. Downward particle Doppler vertical velocities are positive.

was only produced when the wind shifted southwestward, perpendicular to the Canadian Rockies.

Most precipitation events associated with eastward moisture fluxes from the Pacific Ocean brought relatively lower amounts of precipitation to the SPADE domain (events 3 and 11); event 3 was produced by generating cells (not shown). Similarly, small amounts of

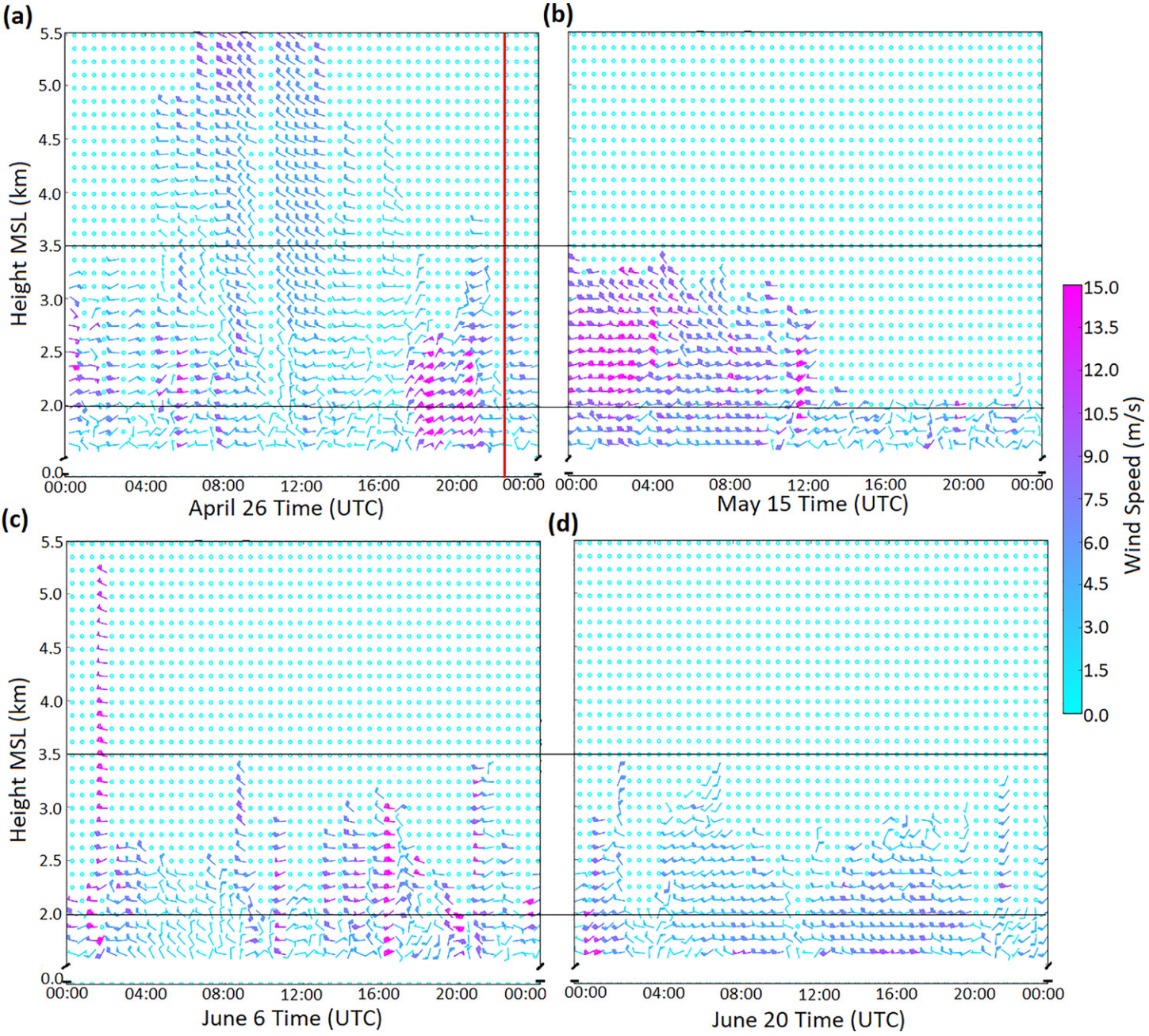

Fig. 8. The 24-h continuous vertical wind profiles from the Fortress Junction Doppler lidar VAD scans on (a) 26 Apr 2019, (b) 15 May 2019, (c) 6 Jun 2019, and (d) 20 Jun 2019, corresponding to times preceding events 1, 5, 9, and 13, respectively. Blank areas represent unavailable data (insufficient lidar signal to process the wind profile or a thick cloud base attenuating the beam). VAD wind profiles provided the local (in-valley, <3.5 km MSL) and synoptic (above-valley > 3.5 km MSL) wind fields preceding the major precipitation events. Black horizontal lines indicate the heights of Fortress Powerline (2 km MSL) and the continental divide (3.5 km MSL). The red vertical line in (a) represents the time that precipitation event 1 took place [not available for (b)–(d)]. Note that event 12 ended only a few hours before event 13 (appendix C).

precipitation were observed on either side of the divide during events 2, 4, 8, and 10, which were associated with a southeastward moisture flux along the Canadian Rockies.

Condensate fluxes. Condensate flux, mainly cloud ice and snow condensate, crossed the divide during only six events (events 1, 3, 5, 9, 12, and 13) over the SPADE domain, although almost no moisture flux crossed the divide during event 1 (Fig. 9). Only a small amount of liquid condensate also crossed during events 9, 12, and 13. The snow condensate crossing the divide in event 13 was produced at higher elevations than during event 1 and was also characterized by a higher precipitation layer (Fig. 7). The condensate crossing the divide

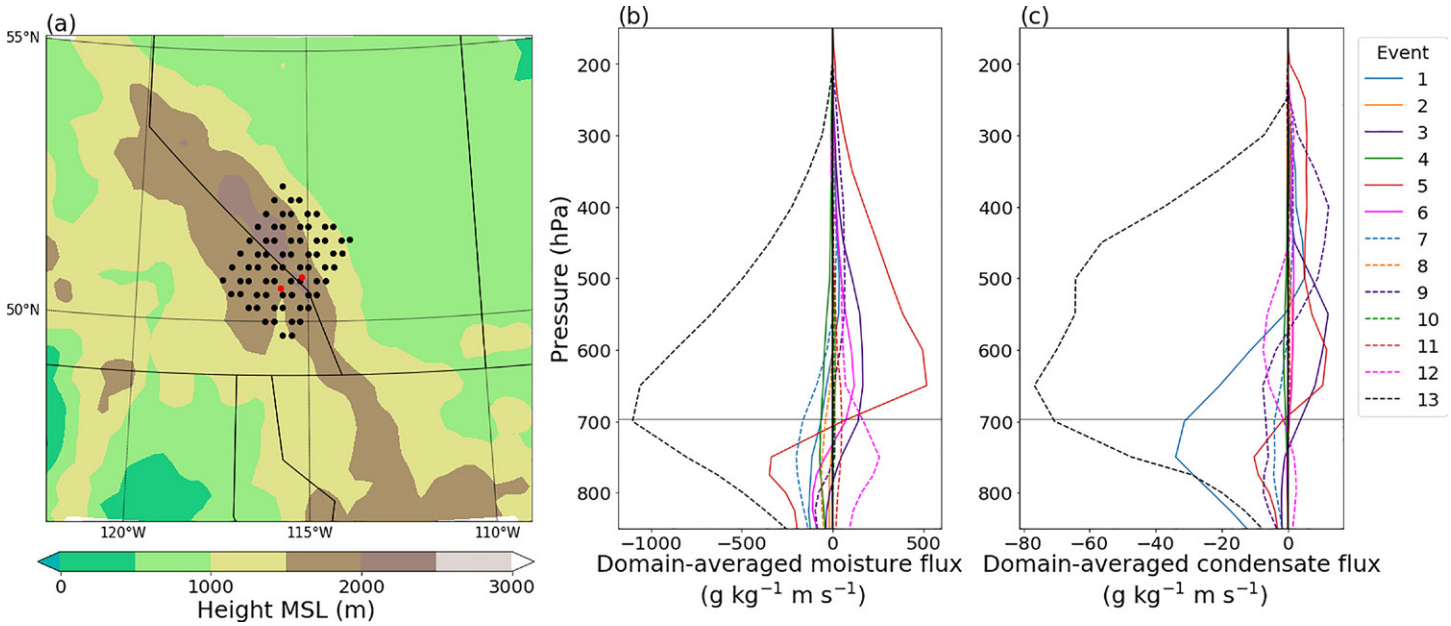

Fig. 9. (a) ERA5 domain (black dots) used to compute the (b) advected moisture and (c) advected condensate fluxes across the continental divide. The fluxes are estimated perpendicular to the continental divide. Red dots show the locations of the stations on both sides of the divide; (b) shows the sum over time of domain-averaged vertical profiles of moisture flux (appendix B) during each event (Table C1); and (c) shows the sum over time of domain-averaged vertical profiles of condensate flux (appendix B) during each event. Positive values are eastward flux whereas negative values are westward flux. Horizontal black lines represent the elevation of the divide (~3 km) in (b) and (c).

during event 1, however, did so predominantly south of Nipika, resulting in a small amount of precipitation being measured at that site (appendix C).

Precipitation condensate aloft was measured by MRRs located on each side of the continental divide (Fig. 10). The reflectivity and particle Doppler velocity profiles were classified into three categories based on the direction of the moisture and condensate fluxes. The most common direction during SPADE was westward fluxes (Table C1), producing the highest amount of precipitation. This could be caused by greater moisture flux convergence when the flow was perpendicular to the mountains, yielding higher precipitation (Mo et al. 2019, 2021). However, strong flows could also lift the precipitation so much that it may pass over the mountain peak (Berg et al. 2017). The three other categories are the southeastward-moving precipitation on the eastern side of the Canadian Rockies, the eastward-moving precipitation on the western side, toward the continental divide, and the northwestward-moving precipitation (not shown in Fig. 10).

During westward moisture flux events, precipitation usually occurred on the eastern slopes before reaching Nipika; event 13 is a good example of such a system. These events were characterized by high occurrences of ice condensate at 7 km MSL, and increasing reflectivity down to ~5 km MSL. At Fortress Powerline, the increase of reflectivity values, in combination with the small increase of particle Doppler vertical velocities at ~1 m s^{-1} indicated ice particles falling, and possible occurrence of aggregation. Some precipitation reaching Nipika during westward moisture fluxes could be related to the spillover of ice condensate over the continental divide as ice particles fall slower than raindrops, hence, could drift farther downwind. Increases in reflectivity from 4 km MSL to the surface at Nipika, coupled with increasing particle Doppler velocities, suggest melting.

Different reflectivity and particle Doppler velocity patterns were measured when the moisture and condensate fluxes moved in the other directions (Fig. 10). These precipitation events produced less precipitation than those moving westward. Southeastward flux events produced virga at Fortress and Nipika (event 8), which is characterized by lower normalized

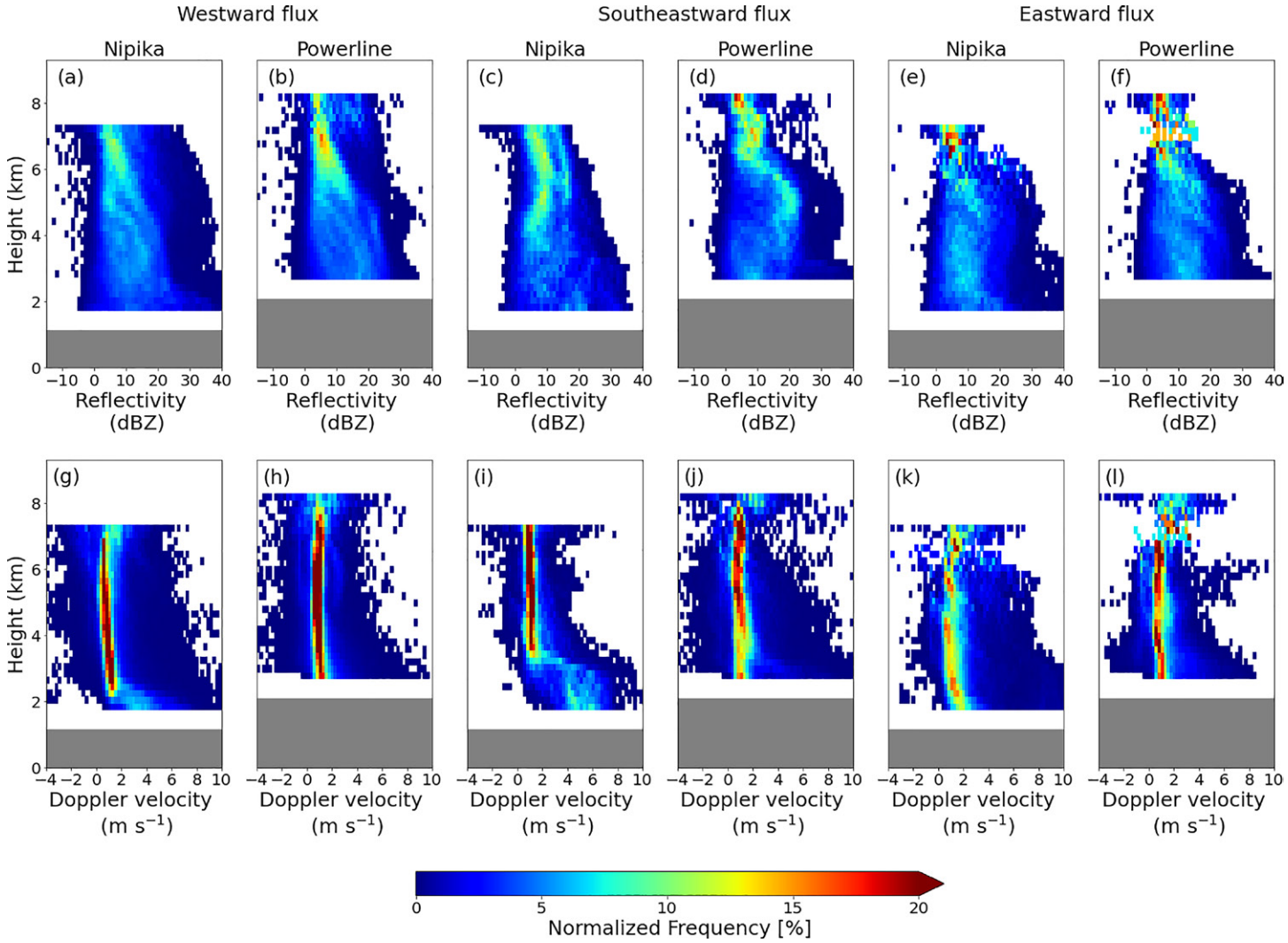

Fig. 10. Normalized contour frequency by altitude diagram (CFAD) of (a)–(f) reflectivity and (g)–(l) particle Doppler velocity from the MRR measurements at Nipika and Fortress Powerline during westward moisture flux in (a), (b), (g), and (h), including events 1, 6, 7, 9, 12, and 13; southeastward moisture flux in (c), (d), (i), and (j), including events 2, 4, 8, and 10; and eastward moisture flux in (e), (f), (k), and (l), including events 3 and 11. MRR measurements during event 5 were not included as this event was the only one with a northwestward moisture flux. Downward particle Doppler vertical velocities are positive.

frequencies in reflectivity (wide range of reflectivity) at ~3 km MSL on both sides of the divide. At that elevation, Doppler velocity increased rapidly downward at Nipika, suggesting melting of solid precipitation that did not sublimate, while snow reached the surface on the eastern side. In contrast, the reflectivity and Doppler velocity patterns suggest solid precipitation melting into rain at lower levels at Nipika during the eastward flux events. Mainly solid precipitation reached the surface at Powerline, which is supported by Doppler velocities ~ 1–2 m s^{-1} and relatively constant reflectivity with height.

Discussion

Precipitation across the continental divide. The examination of the precipitation aloft (Figs. 7 and 10) and the moisture and condensate fluxes (Figs. 6 and 9) during the major precipitation events (e.g., 1, 9 and 13) suggest that precipitation crossed the divide when the precipitation is higher (>6 km MSL), which is well above the divide. For example, if a precipitation event was caused by broad synoptic-scale forcing, it brought a larger amount of moisture over a thicker precipitation layer within the troposphere and precipitation crossed the divide (e.g., event 13). Under different conditions (e.g., event 1), an intense low pressure

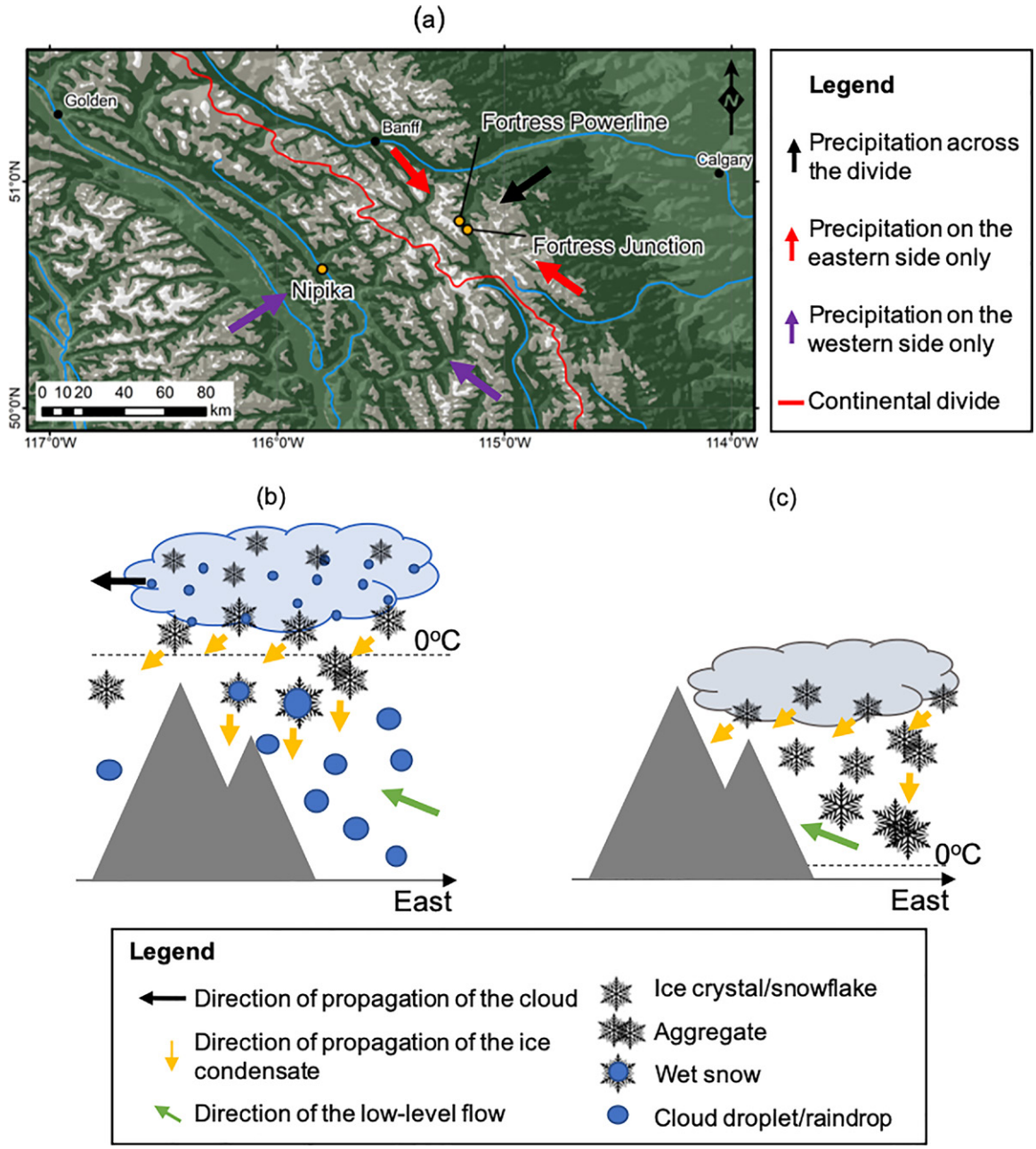

Fig. 11. (a) Map of the study area showing the direction of the moisture flux leading to precipitation across the divide (black arrow), precipitation staying on the east side (red arrows) and precipitation staying on the west side (purple arrows). A summary of the 13 documented storms during SPADE is provided in appendix C. Note that the northwestward arrows are both associated with event 5. (b),(c) Schematic diagrams of the atmospheric conditions and precipitation characteristics when precipitation crossed the divide and when the precipitation did not cross the divide, respectively. In (b), the warmer cloud contains liquid droplets and ice particles, and in (c) the colder cloud mainly consists of ice crystals. The direction of propagation of the cloud and precipitation is shown. The cloud droplets and raindrops are smaller and larger blue circles, respectively.

system in southern AB caused high amounts of orographic precipitation on the eastern side but almost none crossed the divide.

When precipitation crossed the divide, slow-falling ice crystals were probably occurring aloft (Fig. 7). The presence of these particles above the continental divide could be captured by the horizontal wind and transported across the continental divide. This interpretation is supported by the relatively low particle Doppler velocity and MRR reflectivity values, and by the deep precipitation layer above the continental divide (i.e., event 13).

Differences in precipitation characteristics were also observed when precipitation was recorded at both sides of the divide simultaneously (Figs. 4, 5, 7, and 10). By comparing events 1 and 13, precipitation occurred simultaneously across the divide when larger and mixed precipitation particles were observed. This is consistent with the measured deeper precipitation layer, allowing particles to melt or to grow by deposition, aggregation, and riming.

Conceptual model. Based on an examination of all the collected information, it is apparent that the relative amount of precipitation and condensate crossing the divide depended on the weather pattern, precipitation characteristics as well as moisture and condensate fluxes. This insight is pulled together into a conceptual framework that is based on the four synoptic-scale patterns, and related features, that led to precipitation on either side, or both sides, of the continental divide (Fig. 11).

Weather patterns led to moisture flux nearly perpendicular and parallel to the divide. When the moisture flux was perpendicular to the divide, either from the east or the west, more precipitation was produced on the side from which the moisture originated. In addition to the orientation of the moisture flux, precipitation only occurred on both sides when sufficient moisture crossed the divide and when the condensate did not sublimate or evaporate while falling into relatively dry conditions on the other side. In contrast, precipitation never occurred simultaneously on both sides when the moisture flux was nearly parallel to the continental divide and originated from the northwest. When the moisture flux originated from the southeast, it produced precipitation on both sides of the divide without crossing it; the moisture producing precipitation was available on each side of the divide simultaneously.

Whether precipitation did or did not cross the divide also depended on finer-scale processes including condensate features (Fig. 11). For example, during westward flow fields, particles were slightly larger at Fortress Powerline when precipitation crossed the divide. This is consistent with deeper precipitation layers over Fortress, favoring hydrometeor drift and spillover across the divide (Mo et al. 2019), as well as particle growth by deposition, aggregation, and riming (Kim et al. 2021). Deep precipitation layers also occurred during events with higher available moisture for diffusional growth and when slow-falling particles aloft melted into mixed precipitation and rain.

The deeper precipitation layer produced ice crystals aloft (>5 km MSL), which were advected to the other side of the mountain range. The side onto which precipitation particles fall also depends on the growth time (Houze 2012). If particles are denser upstream of the divide, they will likely fall on the same side. In contrast, pristine ice crystals aloft are advected to the other side as they continue to grow by deposition, riming, and aggregation. Additionally, the drier conditions on the western side slows down the melting process but not enough to produce solid precipitation at the surface. Findings are consistent with Zagrodnik et al. (2021) over the Olympic Mountains with the moisture and flow field coming from the east and the continental interior instead of from the west and the Pacific Ocean.

Concluding remarks

SPADE addressed key questions related to water availability and processes associated with water partitioning at a major continental divide. Thirteen precipitation events occurred over a 2-month period from 24 April to 26 June 2019. The ensuing analyses have led to the development of a conceptual model for the occurrence of precipitation across the continental divide. This conceptual model incorporates numerous driving factors including weather patterns, vertical air motions as well as particle size, phase, and density.

It is recognized that these conditions are based on observations over a relatively short period in which in situ sampling was constrained to only three remote sites. Further research, including high-resolution modeling, is needed to precisely assess atmospheric conditions

leading to precipitation crossing the divide. Future efforts should also explore the degree to which our findings are applicable to other snowmelt seasons and to other periods of the year. Overall, SPADE provides a rich database for improved understanding and model representation of precipitation processes in complex terrain during the snowmelt season and it lays a solid foundation for future field campaigns in the region.

Implications

Several mechanisms, including orographic lifting, the seeder-feeder mechanism and atmospheric stability impact the precipitation gradients along the mountain slopes. A linear regression analysis using nine years and 60 stations located at a variety of sites suggested that elevation explains only half ($R^2 = 0.51$) of the total annual precipitation accumulation, which increases at a rate of 0.39 mm m^{-1} of elevation (Mitchell 2022). This precipitation–elevation relationship vanishes when only the continental divide's western side is considered. This could be explained by the atmospheric patterns leading to variable precipitation in the Canadian Rockies as found in SPADE. Nevertheless, results remain generally consistent with prior efforts showing the importance of elevation on precipitation accumulation in the Canadian Rockies (e.g., Smith 2008).

The process and rate of moisture conversion into condensate is particularly important in mountain areas. Growth processes into various ice crystal habits, which often occurred simultaneously during SPADE and as found previously (Thériault et al. 2018; Poirier et al. 2019), are not yet considered in most atmospheric models. This would affect the particle drift aloft, growth/decay processes along their trajectories, and in turn, the distribution of precipitation at the surface. This could in part explain, for instance, substantial biases in simulated precipitation using 4-km grid spacing, with major implications for hydrological modeling (Fang and Pomeroy 2019).

Local water cycling is impacted by these precipitation-related mechanisms because surface water is being redistributed among major drainage basins. For example, moisture from the Canadian Prairies would lead to precipitation that can cross the continental divide and flow into the Pacific Ocean instead of remaining within the same drainage basin. This would have significant implications on water availability across the often dry Canadian Prairies.

Finally, water distribution across the continental divide may be substantially impacted by climate change. Assuming no difference in wind speed, warmer and more moist conditions may lead to deeper precipitation layers and consequently enhancing precipitation crossing the divide. In contrast, these warmer conditions would also produce more fast-falling rain leading to reduced horizontal transport, and in turn, to reduced precipitation crossing the divide.

Acknowledgments. Funding was provided by the Canada First Research Excellence Fund's Global Water Futures programme (GWF), NSERC Discovery Grants (Julie M. Thériault, Stephen J. Déry, John W. Pomeroy, and Ronald E. Stewart), the Canada Research Chairs Program (Julie M. Thériault, John W. Pomeroy), UNBC (Selina Mitchell), NSERC CGS-M, and a FRQNT fellowship (Aurélie Desroches-Lapointe) to conduct scientific analysis. Some instruments, particularly those at Fortress Mountain Snow Laboratory and Nipika Mountain Resort were acquired through the Canada Foundation for Innovation (CFI) Innovation programme. Thanks to Cécile Carton (UQAM) and Jeremy Morris (UNBC), Robin Heavens, Greg Galloway, Lindsey Langs, and the other researchers from the U. Saskatchewan Centre for Hydrology in Canmore who contributed during the field campaign; Adrienne Cunnings, Michelle Ives, and the staff at the University of Calgary Biogeoscience Institute; Lyle and Dianne Wilson and the staff at Nipika Mountain Resort, Fortress Mountain Resort, Fortress Junction Service, and Storm Mountain Lodge; and Shawn Marshall (U. Calgary and ECCC) for their help with project initiation. The authors acknowledge the contribution of Environment and

Climate Change Canada (ECCC) Observation-based Research Section to this work as well as Robert Reed and Michael Harwood for assisting with the deployment of the ECCC instruments. Finally, the authors thank two UQAM graduate students (Mathieu Lachapelle, Benjamin Serralheiro-O'Neill) for their assistance with the review process as well as the two anonymous referees and the editor for constructive comments.

Data availability statement. The data used to conduct this research are described in Thériault et al. (2021). The data were deposited in the publicly accessible Federated Research Data Repository (FRDR; doi.org/10.20383/101.0221).

Appendix A: Micro Rain Radar and the optical-laser disdrometer data analysis

The Micro Rain Radar data are postprocessed following Maahn and Kollias (2012) to improve data quality for solid precipitation. The spectra and particle Doppler velocity data were recorded every 10 s, and within 31 range gates, ranging from 200 to 6,200 m above ground level with a vertical resolution of 200 m for Fortress Powerline and Nipika, and from 35 to 1,085 m MSL with a vertical resolution of 35 m for Fortress Junction.

The optical-laser disdrometer recorded at 1-min interval the number of hydrometeors within 32 diameter bins and 32 fall speed bins, ranging from 0.062 to 24.5 mm (midclass values) and from 0.05 to 20.8 m s^{-1} (midclass values), respectively. The weighted average fall speed in each diameter bin was estimated based on measured particle count. The 1-min samples of weighted average fall speed were then classified as dry snow, wet/rimed snow, and rain by finding the closest empirical fall speed–diameter relationship (Rasmussen et al. 1999; Ishizaka et al. 2013). Only hydrometeors with diameters > 1 mm and fall speeds < 40% above which raindrop falls were considered (Yuter et al. 2006).

Appendix B: Moisture and condensate flux calculation

The moisture flux at each pressure level ($\mathbf{q}_{\text{adv}}$ in g kg^{-1} m s^{-1}) and condensate flux at each pressure level ($\mathbf{q}_{\text{cadv}}$ in g kg^{-1} m s^{-1}) were calculated as follows:

$$(\mathbf{q}_{\text{adv}}, \mathbf{q}_{\text{cadv}}) = q\mathbf{V}, q_c\mathbf{V}, \tag{B1}$$

where q and q_c are the water vapor and condensed water mass mixing ratios (g kg^{-1}), respectively, and $\mathbf{V}$ is the horizontal wind vector at each pressure level (m s^{-1}). From these fluxes, the vertically integrated moisture flux ($\mathbf{Q}$ in kg m^{-1} s^{-1}), and the vertically integrated condensate flux ($\mathbf{Q}_c$ in kg m^{-1} s^{-1}) were determined (e.g., Mo et al. 2019):

$$(\mathbf{Q}, \mathbf{Q}_c) = 10^{-3} g^{-1} \int_{p_o}^{p_t} (\mathbf{q}_{\text{adv}}, \mathbf{q}_{\text{cadv}})\, dp, \tag{B2}$$

where g is gravitational acceleration (m s^{-2}), p is the pressure (Pa), and p_0 and p_t are the pressures at the surface and at the top of the air column (Pa), respectively. The magnitude of $\mathbf{Q}$ is referred to as the integrated water vapor transport (IVT; in kg m^{-1} s^{-1}) and the magnitude of $\mathbf{Q}_c$ is referred to as the integrated condensate transport (ICT; in kg m^{-1} s^{-1}).

Appendix C: Summary of documented precipitation events

A summary of the meteorological conditions on both sides of the continental divide during the 13 SPADE events is given in Table C1.

The duration of the events was based on the timing of the manual observations and whether a period of <6 h occurred between two events. The amounts of precipitation were obtained from the weighing precipitation gauges at each site. The type of precipitation

Table C1. Summary of the 13 precipitation events recorded between 24 Apr and 26 Jun 2019. No. is the number of the event, start time is the time and day in 2019 at which the event started, Pcpn is precipitation, T_m is the mean air temperature, RH_m is the mean relative humidity, and the eighth column is a general description of the synoptic-scale conditions. The three rows in the Pcpn amount, Pcpn phase (where R = rain, S = snow, M = mixed), T_m, and RH_m correspond to each of the three SPADE sites. From west to east, the first row is Nipika, the second is Fortress Powerline, and the third is Fortress Junction. AR means atmospheric river.

No.	Start time	Duration (h)	Pcpn amount (mm)	Pcpn phase	T_m (°C)	RH_m (%)	Moisture flux direction/associated with AR
1	2250 UTC 26 Apr 2019	36.17	3.2	R	2.7	76.2	Westward/no
			32.5	S	−5.4	86.5	
			10.7	M	−1.4	81.2	
2	1900 UTC 30 Apr 2019	6.5	0.1	—	6.6	31.5	Southeastward/no
			4.2	S	−5.8	79.5	
			0.6	S	−1.6	68.2	
3	1700 UTC 4 May 2019	18.33	2.3	R	9.4	58.7	Eastward/prior to AR
			15.3	S	−4.7	91.2	
			7.6	S	−1.2	87.2	
4	1800 UTC 8 May 2019	6	0.6	—	16.3	25.2	Southeastward/after AR
			1.2	S	2.6	66.5	
			0.0	—	7.4	53.7	
5	0500 UTC 16 May 2019	65.5	14.9	R	8.4	83.1	Northwestward/after AR
			20.2	M	−0.5	95.7	
			9.5	M	3.0	89.4	
6	0445 UTC 24 May 2019	18.5	3.5	R	9.7	75.0	Westward/no
			8.5	M	3.2	89.9	
			5.3	R	6.3	87.9	
7	1220 UTC 25 May 2019	11.33	2.3	R	10.4	81.3	Westward/no
			14.5	M	0.4	95.1	
			10.3	R	4.3	90.7	
8	1600 UTC 30 May 2019	6.17	1.0	R	11.8	90.1	Southeastward/no
			6.5	R	7.8	77.2	
			1.6	R	10.6	89.6	
9	0100 UTC 7 Jun 2019	25	15.8	R	6.5	92.3	Westward/prior to AR
			21.4	M	0.1	93.1	
			12.1	M	3.2	87.9	
10	1010 UTC 14 Jun 2019	0.5	0.0	—	10.6	98.2	Southeastward/prior to AR
			1.3	R	5.9	88.2	
			1.0	R	9.7	82.6	
11	2000 UTC 17 Jun 2019	3.83	0.6	R	25.2	30.2	Eastward/after AR
			1.1	R	12.1	61.5	
			0.8	R	15.9	56.7	
12	0830 UTC 19 Jun 2019	35.17	6.2	R	8.5	78.0	Westward/no
			12.6	M	2.3	79.8	
			3.4	R	5.7	76.6	
13	0330 UTC 21 Jun 2019	20.17	20.5	R	6.7	88.0	Westward/no
			56.0	M	1.6	96.6	
			70.2	M	1.6	96.3	

was obtained from the manual observations, which compared well with the optical-laser disdrometer precipitation type diagnostic explained in appendix B.

SPADE documented four events that produced more than 20 mm at Fortress Powerline. These are events 1, 5, 9, and 13. Events 1, 9, and 13 were associated with a low pressure system located over the Canadian Prairies. In contrast, the precipitation during event 5 was associated with moisture fluxes traveling northward along the Rockies to the SPADE sites. The moisture originally came from an atmospheric river landfall on the coast of California. During this event, the flow of moisture and condensate was mainly parallel to, and covered both sides of the divide.

The average measured air temperature during May and June at Nipika was 10.9°C, whereas it was 5.1° and 7.4°C at Fortress Junction and Fortress Powerline, respectively. However, given the elevation difference, the air temperatures at Fortress Junction and Fortress Powerline were estimated at the Nipika elevation, which was used as a reference (1,087 m MSL). The average air temperature was similar at all three sites using a 6°C km^{-1} moist adiabatic lapse rate and warmer conditions on the eastern side using the 10°C km^{-1} dry adiabatic lapse rate. These values, however, vary from storm to storm. Up to seven storms were associated with colder conditions on the eastern side using the 6°C km^{-1} lapse rate.

References

Angulo-Martínez, M., S. Beguería, B. Latorre, and M. Fernández-Raga, 2018: Comparison of precipitation measurements by OTT Parsivel2 and Thies LPM optical disdrometers. *Hydrol. Earth Syst. Sci.*, **22**, 2811–2837, https://doi.org/10.5194/hess-22-2811-2018.

Battaglia, A., E. Rustemeier, A. Tokay, U. Blahak, and C. Simmer, 2010: PARSIVEL snow observations: A critical assessment. *J. Atmos. Oceanic Technol.*, **27**, 333–344, https://doi.org/10.1175/2009JTECHA1332.1.

Bentley, W. A., and W. J. Humphreys, 1962: *Snow Crystals.* Dover, 224 pp.

Berg, H. W. S., R. E. Stewart and P. Joe, 2017: The characteristics of precipitation observed over Cypress Mountain during the SNOW-V10 campaign. *Atmos. Res.*, **197**, 356–369, https://doi.org/10.1016/j.atmosres.2017.06.009.

Browning, K. A., and R. Wexler, 1968: The determination of kinematic properties of a wind field using Doppler radar. *J. Appl. Meteor. Climatol.*, **7**, 105–113, https://doi.org/10.1175/1520-0450(1968)007<0105:TDOKPO>2.0.CO;2.

Environment and Climate Change Canada, 2021: Canadian climate normals. Government of Canada, https://climate.weather.gc.ca/climate_normals/index_e.html.

Fang, X., and J. W. Pomeroy, 2020: Diagnosis of future changes in hydrology for a Canadian Rockies headwater basin. *Hydrol. Earth Syst. Sci*., **24**, 2731–2754, https://doi.org/10.5194/hess-24-2731-2020.

Flesch, T. K., and G. W. Reuter, 2012: WRF Model simulation of two Alberta flooding events and the impact of topography. *J. Hydrometeor.*, **13**, 695–708, https://doi.org/10.1175/JHM-D-11-035.1.

Garrett, T. J., C. Fallgatter, K. Shkurko, and D. Howlett, 2012: Fall speed measurement and high-resolution multi-angle photography of hydrometeors in free fall. *Atmos. Meas. Tech.*, **5**, 2625–2633, https://doi.org/10.5194/amt-5-2625-2012.

Girard, C., and Coauthors, 2014: Staggered vertical discretization of the Canadian Environmental Multiscale (GEM) model using a coordinate of the log-hydrostatic-pressure type. *Mon. Wea. Rev.*, **142**, 1183–1196, https://doi.org/10.1175/MWR-D-13-00255.1.

Harder, P., and J. W. Pomeroy, 2013: Estimating precipitation phase using a psychrometric energy balance method. *Hydrol. Processes*, **27**, 1901–1914, https://doi.org/10.1002/hyp.9799.

Hersbach, H., and Coauthors, 2020: The ERA5 global reanalysis. *Quart. J. Roy. Meteor. Soc.*, **146**, 1999–2049, https://doi.org/10.1002/qj.3803.

Houze, R. A., Jr., 2012: Orographic effects on precipitating clouds. *Rev. Geophys.*, **50**, RG1001, https://doi.org/10.1029/2011RG000365.

——, and Coauthors, 2017: The Olympic Mountains Experiment (OLYMPEX). *Bull. Amer. Meteor. Soc.*, **98**, 2167–2188, https://doi.org/10.1175/BAMS-D-16-0182.1.

Isaac, G. A., and Coauthors, 2014: Science of Nowcasting Olympic Weather for Vancouver 2010 (SNOW-V10), 2012: A World Weather Research Programme project. *Pure Appl. Geophys.*, **171**, 1–24, https://doi.org/10.1007/s00024-012-0579-0.

Ishizaka, M., H. Motoyoshi, S. Nakai, T. Shiina, T. Kumakura, and K. Muramoto, 2013: A new method for identifying the main type of solid hydrometeors contributing to snowfall from measured size-fall speed relationship. *J. Meteor. Soc. Japan*, **91**, 747–762, https://doi.org/10.2151/jmsj.2013-602.

Kim, K., W. Bang, E.-C. Chang, F. J. Tapiador, C.-L. Tsai, E. Jung, and G. Lee, 2021: Impact of wind pattern and complex topography on snow microphysics during International Collaborative Experiment for PyeongChang 2018 Olympic and Paralympic winter games (ICE-POP 2018). *Atmos. Chem. Phys.*, **21**, 11 955–11 978, https://doi.org/10.5194/acp-21-11955-2021.

Kobayashi, T., 1957: Experimental research on the snow crystal habit and growth by means of a diffusion cloud chamber. *J. Meteor. Soc. Japan*, **35A**, 38–47, https://doi.org/10.2151/jmsj1923.35A.0_38.

Kochtubajda, B., and Coauthors, 2016: The June 2013 Alberta catastrophic flooding event—Part 2: Fine-scale precipitation and associated features. *Hydrol. Processes*, **30**, 4917–4933, https://doi.org/10.1002/hyp.10855.

Kumjian, M. R., K. A. Bowley, P. M. Markowski, K. Lombardo, Z. J. Lebo, and P. Kollias, 2020: Snowflake selfies: A low-cost, high-impact approach toward student engagement in scientific research (with their smartphones). *Bull. Amer. Meteor. Soc.*, **101**, E917–E935, https://doi.org/10.1175/BAMS-D-19-0096.1.

Lhermitte, R. M., and D. Atlas, 1961: Precipitation motion by pulse Doppler radar. *Proc. Ninth Weather Radar Conf.*, Kansas City, MO, Amer. Meteor. Soc., 218–223.

Liu, A. Q., and Coauthors, 2016: The June 2013 Alberta catastrophic flooding event: Part 1—Climatological aspects and hydrometeorological features. *Hydrol. Processes*, **30**, 4899–4916, https://doi.org/10.1002/hyp.10906.

Lundquist, J., M. Hughes, E. Gutmann, and S. Kapnick, 2019: Our skill in modeling mountain rain and snow is bypassing the skill of our observational networks. *Bull. Amer. Meteor. Soc.*, **100**, 2473–2490, https://doi.org/10.1175/BAMS-D-19-0001.1.

Ma, X., K. Bi, Y. Chen, Y. Chen, and Z. Cheng, 2017: Characteristics of winter clouds and precipitation over the mountains of northern Beijing. *Adv. Meteor.*, **2017**, 3536107, https://doi.org/10.1155/2017/3536107.

Maahn, M., and P. Kollias, 2012: Improved Micro Rain Radar snow measurements using Doppler spectra post-processing. *Atmos. Meas. Tech.*, **5**, 2661–2673, https://doi.org/10.5194/amt-5-2661-2012.

Marwitz, J., 1986: A comparison of winter orographic storms over the San Juan Mountains and the Sierra Nevada. *Precipitation Enhancement—A Scientific Challenge, Meteor. Monogr.*, No. 21, Amer. Meteor. Soc., 109–113, https://doi.org/10.1175/0065-9401-21.43.109.

McTaggart-Cowan, R., and Coauthors, 2019: Modernization of atmospheric physics parameterization in Canadian NWP. *J. Adv. Model. Earth Syst.*, **11**, 3593–3635, https://doi.org/10.1029/2019MS001781.

Minder, J. R., D. R. Durran, and G. H. Roe, 2011: Mesoscale controls on the mountainside snow line. *J. Atmos. Sci.*, **68**, 2107–2127, https://doi.org/10.1175/JAS-D-10-05006.1.

Mitchell, S., 2022: Precipitation gradients across the continental divide in the southern Canadian Rockies. M.S. thesis, Natural Resources and Environmental Studies Program, University of Northern British Columbia, 153 pp.

Mo, R., M. M. Brugman, J. A. Milbrandt, J. Goosen, Q. Geng, C. Emond, J. Bau, and A. Erfani, 2019: Impacts of hydrometeor drift on orographic precipitation: Two case studies of landfalling atmospheric rivers in British Columbia, Canada. *Wea. Forecasting*, **34**, 1211–1237, https://doi.org/10.1175/WAF-D-18-0176.1.

——, and Coauthors, 2021: Column relative humidity and primary condensation rate as two useful supplements to atmospheric river analysis. *Water Resour. Res.*, **57**, e2021WR029678, https://doi.org/10.1029/2021WR029678.

Morales, A., D. J. Posselt, H. Morrison, and F. He, 2019: Assessing the influence of microphysical and environmental parameter perturbations on orographic precipitation. *J. Atmos. Sci.*, **76**, 1373–1395, https://doi.org/10.1175/JAS-D-18-0301.1.

Moran, T., S. J. Marshall, E. C. Evans, and K. E. Sinclair, 2007: Altitudinal gradients of stable isotopes in lee-slope precipitation in the Candian Rocky Mountains. *Arct. Antarct. Alp. Res.*, **39**, 455–467, https://doi.org/10.1657/1523-0430(06-022)[MORAN]2.0.CO;2.

Nakaya, U., 1954: *Snow Crystals: Natural and Artificial.* Harvard University Press, 510 pp., https://doi.org/10.1126/science.120.3123.755.a.

Poirier, É., J. M. Thériault, and M. Leriche, 2019: Role of sublimation and riming in the precipitation distribution in the Kananaskis valley, Alberta, Canada. *Hydrol. Earth Syst. Sci.*, **23**, 4097–4111, https://doi.org/10.5194/hess-23-4097-2019.

Pomeroy, J. W., R. E. Stewart, and P. H. Whitfield, 2016a: The 2013 flood event in the South Saskatchewan and Elk River basins: Causes, assessment and damage. *Can. Water Resour. J.*, **41**, 105–117, https://doi.org/10.1080/07011784.2015.1089190.

——, X. Fang, and D. G. Marks, 2016b: The cold rain-on-snow event of June 2013 in the Canadian Rockies—Characteristics and diagnosis. *Hydrol. Processes*, **30**, 2899–2914, https://doi.org/10.1002/hyp.10905.

Rasmussen, R. M., J. Vivekanandan, J. Cole, B. Meyers, and C. Masters, 1999: The estimation of snowfall rate using visibility. *J. Appl. Meteor. Climatol.*, **38**, 1542–1563, https://doi.org/10.1175/1520-0450(1999)038<1542:TEOSRU>2.0.CO;2.

Rood, S. B., G. M. Samuelson, J. K. Weber, and K. A. Wywrot, 2005: Twentieth-century decline in streamflows from the hydrographic apex of North America. *J. Hydrol.*, **306**, 215–233, https://doi.org/10.1016/j.jhydrol.2004.09.010.

Sharma, A., and S. J. Déry, 2020: Contribution of atmospheric rivers to annual, seasonal, and extreme precipitation British Columbia and southeastern Alaska. *J. Geophys. Res. Atmos.*, **125**, e2019JD031823, https://doi.org/10.1029/2019JD031823.

Sinclair, K. E., and S. J. Marshall, 2009: Temperature and vapour-trajectory controls on the stable-isotope signal in the Canadian Rocky Mountain snowpacks. *J. Glaciol.*, **55**, 485–497, https://doi.org/10.3189/002214309788816687.

Smith, C. D., 2008: The relationship between monthly precipitation and elevation in the Alberta foothills during the Foothills Orographic Precipitation Experiment. *Cold Region Atmospheric and Hydrologic Studies: The Mackenzie GEWEX Experience*, M. Woo, Ed., Springer, 167–183.

Steiner, M., O. Bousquet, R. A. Houze Jr., B. F. Smull, and M. Mancini, 2003: Airflow within major Alpine river valleys under heavy rainfall. *Quart. J. Roy. Meteor. Soc.*, **129**, 411–431, https://doi.org/10.1256/qj.02.08.

Stoelinga, M. T., and Coauthors, 2003: Improvement of Microphysical Parameterization through Observational Verification Experiment. *Bull. Amer. Meteor. Soc.*, **84**, 1807–1826, https://doi.org/10.1175/BAMS-84-12-1807.

Tessendorf, S. A., and Coauthors, 2018: A transformational approach to winter orographic weather modification research. *Bull. Amer. Meteor. Soc.*, **100**, 71–92, https://doi.org/10.1175/BAMS-D-17-0152.1.

Thériault, J. M., I. Hung, P. Vaquer, R. Stewart, and J. Pomeroy, 2018: Precipitation characteristics and associated weather conditions on the eastern slopes of the Canadian Rockies during March–April 2015. *Hydrol. Earth Syst. Sci.*, **22**, 4491–4512, https://doi.org/10.5194/hess-22-4491-2018.

——, and Coauthors, 2021: Meteorological observations collected during the Storms and Precipitation Across the continental Divide Experiment (SPADE), April–June 2019. *Earth Syst. Sci. Data*, **13**, 1233–1249, https://doi.org/10.5194/essd-13-1233-2021.

Vionnet, V., V. Fortin, E. Gaborit, G. Roy, M. Abrahamowicz, N. Gasset, and J. W. Pomeroy, 2020: Assessing the factors governing the ability to predict late-spring flooding in cold-region mountain basins. *Hydrol. Earth Syst. Sci.*, **24**, 2141–2165, https://doi.org/10.5194/hess-24-2141-2020.

Whitfield, P. H., and J. W. Pomeroy, 2016: Changes to flood peaks of a mountain river: Implications for analysis of the 2013 flood in the Upper Bow River, Canada. *Hydrol. Processes*, **30**, 4657–4673, https://doi.org/10.1002/hyp.10957.

Yuter, S. E., D. E. Kingsmill, L. B. Nance, and M. Löffler-Mang, 2006: Observations of precipitation size and fall speed characteristics within coexisting rain and wet snow. *J. Appl. Meteor. Climatol.*, **45**, 1450–1464, https://doi.org/10.1175/JAM2406.1.

Zagrodnik, J. P., L. McMurdie, and R. Conrick, 2021: Microphysical enhancement processes within stratiform precipitation on the barrier and sub-barrier scale of the Olympic Mountains. *Mon. Wea. Rev.*, **149**, 503–520, https://doi.org/10.1175/MWR-D-20-0164.1.